1997ASPC..123..314H

12th 'Kingston meeting': Computational Astrophysics
ASP Conference Series Vol. 123, 1997
David A. Clarke & Michael J. West (eds.)

Head-on Collisions of Two Black Holes

D. W. Hobill

Department of Physics and Astronomy, University of Calgary, Calgary, AB T2N 1N4, Canada

P. Anninos, H. E. Seidel, L. L. Smarr

NCSA, University of Illinois at Urbana-Champaign, Urbana, IL 61801, U.S.A.

W.-M. Suen

Department of Physics, Washington University, St. Louis, MO 63130, U.S.A.

Abstract. Computations of head-on collisions between two equal-mass black holes are performed by constructing numerical solutions to the Einstein equations. The gravitational waves generated from the dynamics are extracted from the time-dependent metric and these give pulse profiles that should be measured by gravitational wave detectors.

1. Introduction

Some of the best known predictions of general relativity are those associated with the existence of both black holes and gravitational radiation, neither of which have been observed directly. Therefore, one of the great challenges to experimental relativity is to provide unambiguous evidence for the existence of such phenomena. The challenge to computational relativity is to provide unambiguous predictions of effects that should be observable.

A first step in understanding dynamical black hole and gravitational wave spacetimes is described in this paper. While exactly head-on collisions between two equal-mass black holes is rather unlikely, the results reported here do provide some information about dynamical black holes and strong gravitational waves. In addition, the results will provide an important test bed calculation for the more general computations discussed by Choptuik in these proceedings.

2. Splitting Spacetime into Space and Time

Using the method of Arnowitt *et al.* (1962, hereafter ADM), one "slices" the four-dimensional spacetime into three-dimensional spatial hypersurfaces (3-D volumes) threaded together by timelike curves whose tangent vectors determine a "time" vector. This splitting leads to a line element for the "distance" between

© Astronomical Society of the Pacific • Provided by the NASA Astrophysics Data System

1997ASPC..123..314H

infinitesimally separated spacetime points given by:

$$ds^2 = -(\alpha^2 - \beta^i\beta_i)dt^2 + 2\beta_i\, dx^i\, dt + \gamma_{ij}\, dx^i\, dx^j. \quad (1)$$

The Einstein summation notation (*i.e.*, summation is implied over index pairs) is used where the indices, i and j run from 1 to 3 and denote the spatial coordinates (x^1, x^2, x^3). The lapse function, α, determines the interval of proper time, $d\tau$, between the point labeled by t and point labeled by $t + dt$, *i.e.*, $d\tau = \alpha\, dt$. The shift vector, β^i, is the coordinate three-velocity that determines the relative position of the spatial coordinate x^i from one 3-volume to the next. Finally the 3-metric γ_{ij} determines the spatial distances between points that lie entirely within a 3-D volume at a particular moment of time, t.

The lapse function and shift vectors are not dynamic variables (the Einstein equations do not provide evolution equations for them) and the freedom to choose them arbitrarily is often exploited to simplify the evolution equations, avoid spacetime singularities, or stabilize a numerical method.

Defining the *extrinsic* curvature (*i.e.*, the field momentum conjugate to the 3-metric) as $K_{ij} = \nabla_i\beta_j + \nabla_j\beta_i - \partial_t\gamma_{ij}$, where ∇_i is the covariant derivative with respect to γ_{ij}, the vacuum Einstein equations break up into the following sets: 1) the constraints which contain no time derivatives:

$$R - K_{ij}K^{ij} + K^2 = 0\,; \quad \text{Hamiltonian constraint}$$

$$\nabla_j(K^j_i - \delta^j_i K) = 0\,; \quad \text{momentum constraint}$$

and 2) the evolution equations for the 3-metric and extrinsic curvature:

$$\partial_t\gamma_{ij} = -2\alpha K_{ij} + \nabla_i\beta_j + \nabla_j\beta_i;$$

$$\partial_t K_{ij} = -\nabla_i\nabla_j\alpha + \alpha(R_{ij} + K_{ij}K - 2K_{ik}K^k_j) + \beta^k\nabla_k K_{ij} + K_{kj}\nabla_i\beta^k + K_{ik}\nabla_j\beta^k;$$

where the the *intrinsic* 3-curvature R_{ik} is determined in the standard Riemannian method from the metric γ_{ik}. The scalar 3-curvature is $R = \gamma^{ij}R_{ij}$ and the trace of the extrinsic curvature is defined by $K = \gamma^{ij}K_{ij}$. The constraint equations form a coupled set of elliptic equations and the evolution equations are hyperbolic equations describing the propagation of the gravitational field.

The construction of a numerical solution to these equations proceeds as follows. First one must choose a convenient coordinate parameterization in order to provide a basis for discretizing space and time. Once a computational grid is established, the partial derivatives appearing in the constraint and evolution equations can be approximated by finite differences.

The constraint equations are solved in the initial 3-volume defined at $t = 0$ for those components of the metric and extrinsic curvature that cannot be freely specified. The solutions to the constraints are then used to provide the right-hand-sides of the evolution equations which determine the metric and extrinsic curvature on the succeeding slice of spacetime. This provides the necessary data to evolve to the next time step via an explicit time-stepping algorithm.

© Astronomical Society of the Pacific • Provided by the NASA Astrophysics Data System

1997ASPC..123..314H

3. Coordinates and Variables for Axisymmetric Spacetimes

The spacetimes to be studied are axially symmetric. Therefore all variables are independent of an azimuthal angle, ϕ. Using standard ($x^1 = z$, $x^2 = \rho$, $x^3 = \phi$) cylindrical coordinates, the general axisymmetric 3-metric can be written as:

$$\gamma_{ij} = \Psi^4 \hat{\gamma}_{ij} = \Psi^4 \begin{pmatrix} a & c & 0 \\ c & b & 0 \\ 0 & 0 & \rho^2 d \end{pmatrix}. \tag{2}$$

The variables a, b, c and d are functions of the coordinates z, ρ and t and are assumed to be asymptotically flat. The conformal factor Ψ is a function of z and ρ only and does not evolve in time—it is determined on the initial time slice from a solution of the Hamiltonian constraint. For the two-black hole collision, Ψ can be computed analytically (see below). On the initial time slice, the 3-metric is conformally flat so, $a = b = d = 1$, and $c = 0$.

The Einstein equations are simplified when a conformal factor is introduced into the extrinsic curvature in a manner similar to the 3-metric [equation (2)],

$$K_{ij} = \Psi^4 \hat{K}_{ij} = \Psi^4 \begin{pmatrix} h_a & h_c & 0 \\ h_c & h_b & 0 \\ 0 & 0 & \rho^2 h_d \end{pmatrix}. \tag{3}$$

The evolution equations can now be formulated as dynamical equations for the variables (a, b, c, d) and (h_a, h_b, h_c, h_d).

4. Misner Initial Data

The initial data for the collision are based on the results of Misner (1960) who constructed a pure vacuum solution to the Hamiltonian constraint equation when $K_{ij} = 0$ (*i.e.*, a time-symmetric solution) and when the metric [equation (2)] is conformally flat. The solution contains two asymptotically flat sheets joined by two throats. This models provides a mathematically precise isometry between the interiors of the black holes and their exteriors.

The conformal factor Ψ_M defined by

$$\Psi_M = 1 + \sum_{n=1}^{\infty} \frac{1}{\sinh(n\mu)} \left(\frac{1}{{}^{+}r_n} + \frac{1}{{}^{-}r_n} \right), \quad \text{where} \quad {}^{\pm}r_n = \sqrt{\rho^2 + [z \pm \coth(n\mu)]^2}$$

solves the Hamiltonian constraint. This data set represents two equal-mass non-rotating black holes initially at rest where the two black hole centers are aligned along the axis of symmetry (z-axis). The free parameter μ is related to the physical parameters, M (half the total asymptotic or ADM mass) and L (the proper distance along the spacelike geodesic connecting the throats) by

$$M = 2 \sum_{n=1}^{\infty} \frac{1}{\sinh(n\mu)}, \qquad L = 2 \left[1 + 2\mu \sum_{n=1}^{\infty} \frac{n}{\sinh(n\mu)} \right].$$

The effect of increasing μ is to set the two black holes further away from one another and decrease the total mass of the system.

© Astronomical Society of the Pacific • Provided by the NASA Astrophysics Data System

1997ASPC..123..314H

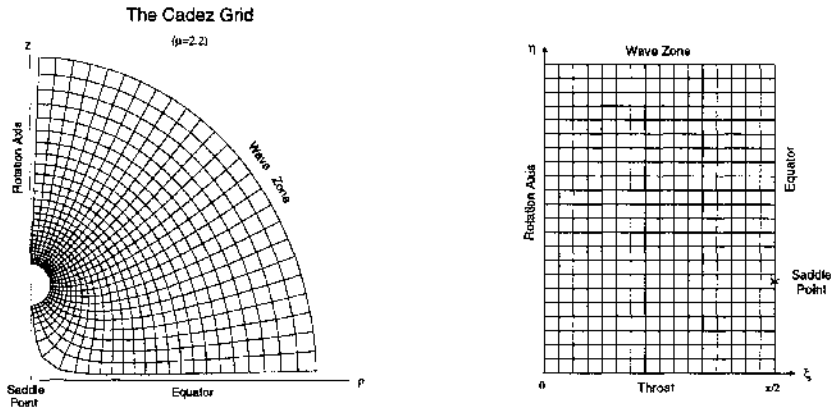


Figure 1. (*left*) The Čadež grid for the case $\mu = 2.2$ and displayed in a single quadrant with cylindrical coordinates. The throats are centered on the symmetry axis at $z = \pm \coth \mu$. (*right*) The computational grid.

5. The Computational Grid

The conformal factor, Ψ_M, assumes that the two black hole throats are spheres, centered on the z-axis. Since the natural boundaries (the throats and a sphere surrounding the system far from the throats) do not lie along constant (z, ρ) coordinates, it is useful to introduce the "quasi-spherical" Čadež (1971) coordinates (η, ξ) with η being a logarithmic "radial" coordinate and ξ an "angular" coordinate. Čadež coordinates are related to cylindrical coordinates through the complex conformal transformation

$$\eta + i\xi = \frac{1}{2}\left[\ln(\zeta + \zeta_0) + \ln(\zeta - \zeta_0)\right] + \sum_{n=1}^{\infty} C_n \left(\frac{1}{(\zeta_0 + \zeta)^n} + \frac{1}{(\zeta_0 - \zeta)^n}\right), \quad (4)$$

where $\zeta = z + i\rho$, and $\zeta_0 = \coth \mu$ is the value of ζ at the throat center. The constant η and ξ coordinate lines lie along the field and equipotential lines of two equally charged metallic cylinders located at $z = \pm \coth \mu$. The coefficients C_n are determined by a least-squares method to set the throats [defined by $\rho_{\rm th}^2 + (z_{\rm th} \pm \coth \mu)^2 = 1/\sinh^2 \mu$] to lie on an $\eta = \eta_0 =$ constant coordinate line. Both η_0 and the different C_n are computed for different μ using this least-squares procedure. The C_n's are rapidly converging and the series in equation (4) can be truncated when $10 \leq n \leq 15$.

The constant Čadež coordinate lines in the cylindrical coordinate system are shown in the left panel of Figure 1. The discretization of the Einstein equations occurs on the rectangular grid shown in the right panel of Figure 1. The advantage afforded by this set of coordinates is that they are spherical both near the throats and far away in the wave zone, thus allowing one to deal with throat boundaries and asymptotic wave form extractions in a convenient way. The disadvantage is that the transformation in equation (4) introduces a singular saddle point at the origin ($z = \rho = 0$) not present in cylindrical coordinates. This creates certain numerical difficulties that are discussed in Anninos *et al.* (1994b).

© Astronomical Society of the Pacific • Provided by the NASA Astrophysics Data System

1997ASPC..123..314H

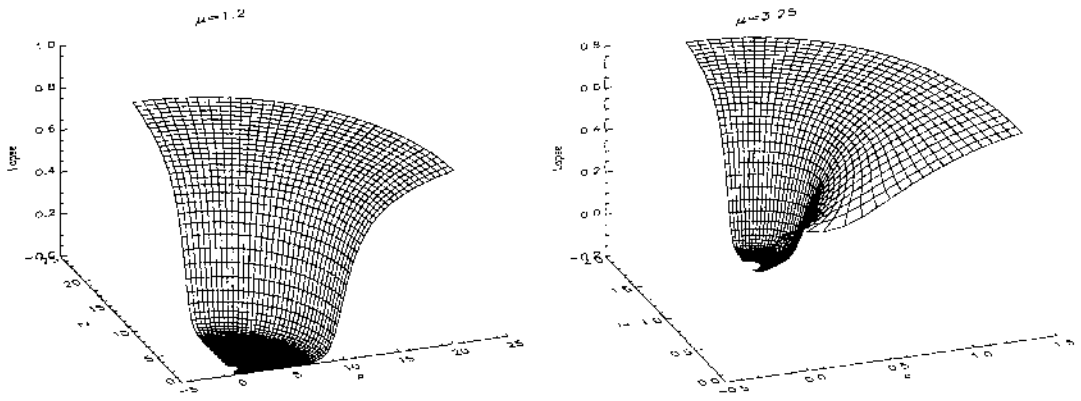


Figure 2. (*left*) The lapse function for the case $\mu = 1.2$ at $t = 24M$. (*right*) The lapse function for $\mu = 3.25$ at $t = 22.5M$

6. Computational Results: The Near Field

The physical attributes of the initial data for six separate Misner two-black-hole data sets are summarized in Table 1, where M represents the mass of a single black hole, and L/M gives the separation between the throats. Also shown is the initial structure of the apparent and event horizons.

μ	M	L/M	Apparent horizon	Event horizon
1.2	1.85	4.46	single	single
1.8	0.81	6.76	separate	critical
2.2	0.50	8.92	separate	separate
2.7	0.29	12.7	separate	separate
3.0	0.21	15.8	separate	separate
3.25	0.16	19.1	separate	separate

Table 1. The physical parameters for initial data sets.

The metric and extrinsic curvature components are computed on each time slice and physically relevant information must be extracted from these quantities. For example, the lapse function for the cases $\mu = 1.2$ ($t = 25M$) and $\mu = 3.25$ ($t = 22.5M$) are shown in the left and right panels of Figures 2 respectively. In the left panel of Figure 2, the lapse goes to zero in the region near the throats, "freezing" all dynamics there. As a result, the proper distance between grid points grows in coordinate time in regions just outside the horizon. This produces a "grid stretching" which presents one of the main difficulties in evolving black hole spacetimes in any numerical simulation utilizing a singularity-avoiding lapse function.

For comparison, the right panel of Figure 2 shows the lapse for the case $\mu = 3.25$ where the throats are much more separated. The initial data consist of two separated horizons. The plot corresponds to an early time in the evolution of the system where the two holes are acting essentially independently of each other as they begin to fall together. After the holes coalesce, the lapse collapses spherically around both throats which are contained within the final black hole.

© Astronomical Society of the Pacific • Provided by the NASA Astrophysics Data System

1997ASPC..123..314H

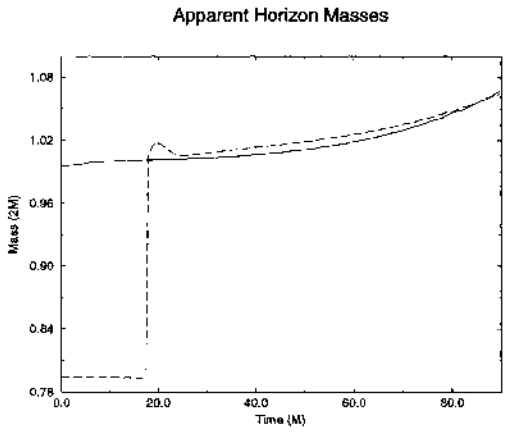


Figure 3. The apparent horizon mass for $\mu = 1.2$ (solid) and $\mu = 2.2$ (dashed). For $\mu = 1.2$ there is a single horizon initially. For $\mu = 2.2$, two horizons exist until $t \approx 17M$ when a single horizon surrounds both holes.

One can define an effective mass of a black hole based on its apparent horizon via the Hawking (1973) relation:

$$M_{\rm h} = \sqrt{A_h/16\pi}, \tag{5}$$

where $A_{\rm h}$ is the intrinsic area of the apparent horizon. This relationship gives a lower limit for the mass of the black hole, since the apparent horizon should lie at or inside the event horizon. When the system is nearly stationary, equation (5) provides a good estimate of the black hole mass as the apparent and event horizons almost coincide (see Anninos, *et al.*, 1994a).

In Figure 3, the evolution of the horizon mass computed from equation (5) is shown for two different cases. The numerical data for the case $\mu = 1.2$ are shown as a solid line. The mass of the hole $M_{\rm h}$ is normalized to units of the total ADM mass of the spacetime, so ideally $M_{\rm h} < 1$ for all time. However, the horizon is always found near the peak of $\tilde{\gamma}_{\eta\eta}$, and therefore M_h is extremely sensitive to the precise position of the horizon. When the horizon lies between grid points, the overestimated surface area results from choosing the outer grid location.

Also shown in Figure 3 is the result for the case $\mu = 2.2$ where the initial horizons are separate and contain only about 79% of the total mass of the spacetime. These surfaces are tracked only until another trapped surface forms across the equator ($z = 0$) to surround both throats.

7. Waveform Extraction and Total Energy Loss

The main method used to calculate waveforms is based on the gauge-invariant extraction technique developed by Abrahams & Evans (1990) and applied in Abrahams *et al.* (1992) to black hole spacetimes. The basic idea is to split the spacetime metric into a spherically-symmetric (static) background and a small perturbation in the region where the curvature is dominated by the mass content

© Astronomical Society of the Pacific • Provided by the NASA Astrophysics Data System

1997ASPC..123..314H

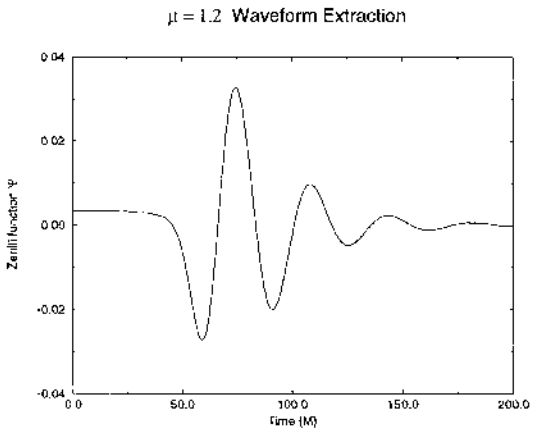


Figure 4. The $\ell = 2$ waveform for the case $\mu = 1.2$ measured at $r = 40M$. The solid line represents the numerical result and the dashed line the fit to the quasi-normal mode perturbation.

of a small compact object. The metric perturbation is expanded in $m = 0$ spherical harmonics $Y_{\ell 0}(\theta)$ and their tensor generalizations. The Regge-Wheeler perturbation functions are then extracted from the numerically computed metric components and used to construct the gauge-invariant Zerilli function ψ. The wavelike part of the metric ψ is radiative at large distances from the source and is commonly used in semi-analytic calculations of black hole normal mode frequencies (*e.g.*, Chandrasekhar, 1983). The asymptotic energy flux carried by gravitational waves can be computed for each ℓ mode contribution from

$$\frac{dE}{dt} = \frac{1}{32\pi}\left(\frac{\partial\psi}{\partial t}\right)^2. \tag{6}$$

For all of the cases studied in this paper, both the $\ell = 2$ and $\ell = 4$ waveforms at radii of 30, 40, 50, 60, and $70M$ have been extracted. By comparing results at each of these radii, the propagation of the waves and the consistency of energy flux calculations can be monitored.

Figure 4 shows the $\ell = 2$ waveform (solid line) extracted at a radius of $40M$ for the case $\mu = 1.2$. A single horizon surrounds both throats in this case and the system evolves as a single perturbed black hole from the outside. Therefore, the radiation is dominated by the quasi-normal modes of the black hole. The dotted line in Figure 4 shows the fit of the lowest two (fundamental and first overtone) $\ell = 2$ modes of a black hole of mass $(2M)$, over the range $70 < t/M < 160$, obtained from Leaver (1985) and Seidel & Iyer (1990). The first overtone quasi-normal mode is more strongly damped than the fundamental, and hence does not contribute appreciably to the fit at late times. Its main effect is to increase the accuracy of the fit to the first peak in the extracted waveform.

Figure 5 shows the $\ell = 2$ and $\ell = 4$ waveforms respectively for the case $\mu = 2.7$. The holes are initially separated by about $12.6M$. The solid lines are the waveforms extracted at a distance $r = 40M$. In this case, the fits to perturbation theory are still reasonably good, but are not as close as the calculations performed for holes that are initially closer together. The wavelengths of the

© Astronomical Society of the Pacific • Provided by the NASA Astrophysics Data System

1997ASPC..123..314H

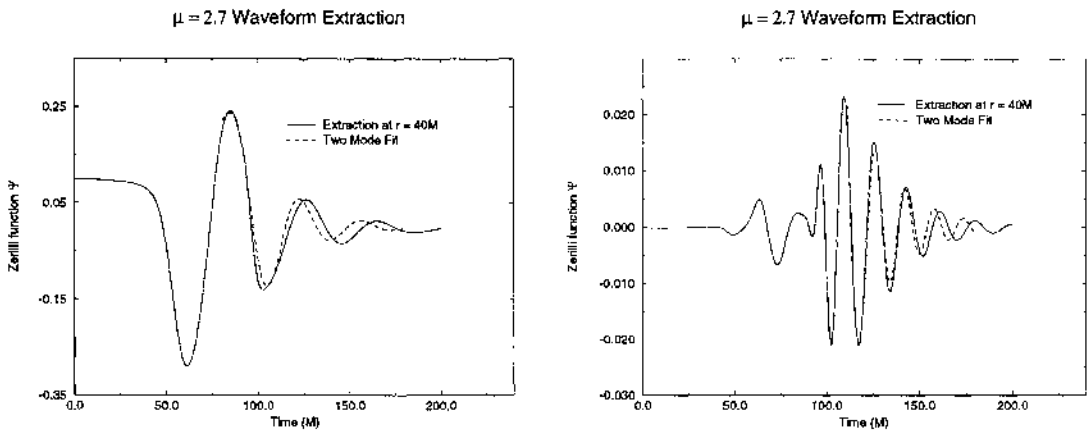


Figure 5. The waveforms for $\mu = 2.7$ measured at $r = 40M$. (*left*) The $\ell = 2$ mode. (*right*) The $\ell = 4$ mode.

extracted waveforms are somewhat too long. The calculation requires a longer period of time before the onset of quasi-normal ringing, so the peak in the radial metric function becomes more difficult to resolve as the accuracy declines. This leads to an error in the effective gravitational scattering potential which is critical in determining the quasi-normal frequencies.

The total radiated energy E can be computed from the Zerilli function using equation (6). The results are shown in Figure 6. The six clusters of unconnected symbols represent the numerical simulations based on the six μ parameter values. Each of the five symbols within a cluster corresponds to the total integrated $\ell = 2$ energy computed at the five different "detector" positions. For reference, the results of Smarr & Eppley (Smarr, 1979) are plotted as x's with error bars based on values suggested by Smarr in his 1979 review. Within the large errors quoted, those early results are remarkably consistent with the results presented here.

The results in Figure 6 show two distinct regimes. For $\mu < 1.8$ (*i.e.*, when $L/M = 6.69$), the initial data contain *one* black hole, and the energy radiated falls off exponentially. For $\mu > 1.8$, there are two holes and the energy radiated is somewhat independent of the initial separation. Finally, we note that the energy radiated is *very* small compared with the upper limits based on the horizon area theorem which are represented by connected circles in Figure 6. More details concerning the energy loss can be found in Anninos *et al.* (1993; 1995). Ultimately, the total energy radiated by these systems is on the order of $0.002M$ (where M is half the ADM mass of the spacetime). This implies that at least for head-on collisions of black holes, such systems cannot be considered to be efficient generators of gravitational radiation.

Acknowledgments. We would like to thank David Bernstein for a number of helpful discussions, Mark Bajuk for his work on visualizations of the numerical simulations that aided greatly in their interpretation, and Joan Massó for help with preparing some of the graphs for this paper. This work was supported by NCSA, NSF Grants 91-16682, 94-04788, 94-07882, ASC/PHY93-18152 (ARPA supplemented), and NSERC Grant No. OGP-121857. The computations were

© Astronomical Society of the Pacific • Provided by the NASA Astrophysics Data System

1997ASPC..123..314H

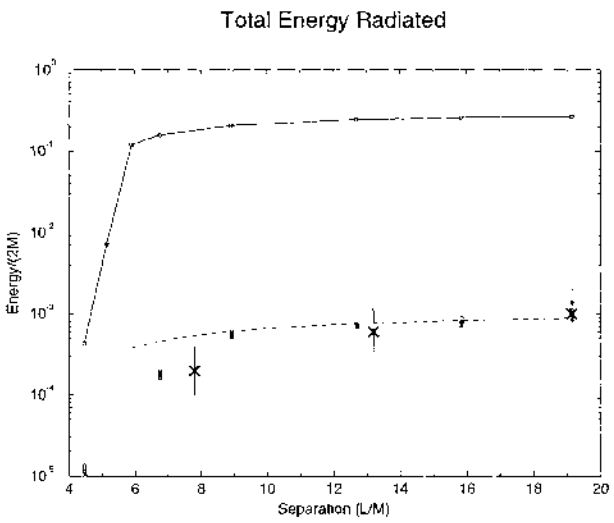


Figure 6. The total gravitational wave energy output for six values of μ as measured at "detectors" located at different fixed radii from the source.

performed at NCSA, the Pittsburgh Supercomputing Center and the Calgary High Performance Computing Center.

References

Abrahams, A., & Evans, C. 1990, Phys. Rev. D, 42, 2585.

Abrahams, A., Bernstein, D., Hobill, D., Seidel, E., & Smarr, L. 1992, Phys. Rev. D, 45, 3544.

Anninos, P., Hobill, D., Seidel, E., Smarr, L., & Suen, W-M. 1993, Phys. Rev. Lett., 71, 2851.

Anninos, P., Bernstein, D., Brandt, S., Hobill, D., Seidel, E., & Smarr, L. 1994a, Phys. Rev. D, 50, 3801.

Anninos, P., Hobill, D., Seidel, E., Smarr, L., & Suen, W-M. 1994b, *Technical Report 024*, (Urbana: National Center for Supercomputing Applications).

Anninos, P., Hobill, D., Seidel, E., Smarr, L., & Suen, W-M. 1995, Phys. Rev. D, 52, 2044.

Arnowitt, R., Deser, S., & Misner, C. W. 1962, in *Gravitation: An Introduction to Current Research*, ed. L. Witten, (New York: John Wiley).

Čadež, A. 1971, Ph.D. thesis, (University of North Carolina, Chapel Hill).

Chandrasekhar, S. 1983, *The Mathematical Theory of Black Holes*, (Oxford: Oxford University Press).

Hawking, S. W. 1973, in *Black Holes*, eds. C. DeWitt & B. S. DeWitt, (New York: Gordon and Breach).

Leaver, E. 1985, Proc. R. Soc. (London), A402, 285.

Misner, C. W. 1960, Phys. Rev., 118, 1110.

Seidel, E., & Iyer, S. 1990, Phys. Rev. D, 4, 374.

Smarr, L. 1979, in *Sources of Gravitational Radiation*, ed. L. Smarr, (Cambridge: Cambridge University Press), 245.

© Astronomical Society of the Pacific • Provided by the NASA Astrophysics Data System

View publication stats